Natural Hazards
and Earth System
Sciences

Discussions

Progressive advance and runout hazard assessment of a low-angle valley glacier in East Kunlun Mountains from multi-sensor satellite imagery analysis

Xiaowen Wang[1, 2], Lin Liu[3], Yan Hu[3], Tonghua Wu[4], Lin Zhao[4, 5], Qiao Liu[6], Rui Zhang[1, 2], Bo Zhang[1], Guoxiang Liu[1, 2]

[1]Faculty of Geosciences and Environmental Engineering, Southwest Jiaotong University, China

5 [2]State-Province Joint Engineering Laboratory of Spatial Information Technology of High-speed Rail Safety, Southwest Jiaotong University, China

[3]Earth System Science Programme, Faculty of Science, The Chinese University of Hong Kong, China

[4]Cryosphere Research Station on the Qinghai-Tibet Plateau, State Key Laboratory of Cryosphere Science, Northwest Institute of Eco-Environment and Resources, Chinese Academy of Sciences, China

10 [5]School of Geographical Sciences, Nanjing University of Information Science and Technology, China

[6]Institute of Mountain Hazards and Environment, Chinese Academy of Sciences, China

Correspondence to: Xiaowen Wang (insarwxw@swjtu.edu.cn)

Abstract: Collapses of large parts of low-angle mountain glaciers in recent years have raised great attention due to their threats to lives and properties downstream. While current studies have mainly focused on post-event analysis, assessing the potential

15 hazard of glaciers prone to collapse is rare. Here we presented a comprehensive analysis of the dynamics and runout hazard of a low-angle (~20°) valley glacier, close to the Qinghai-Tibet railway and highway, in the Kunlun Pass of East Kunlun Mountains on the Qinghai-Tibet Plateau. The changes in morphology, terminus position, and surface elevation of the glacier between 1975 and 2019 were characterized with multi-sensor remote sensing data including a stereo-image pair from the historical KH-9 spy satellite, six Digital Elevation Models (DEMs), and nine high-resolution images from Planet Labs. The

20 surface flow velocities of the glacier tongue between 2009 and 2019 were also tracked based on cross-correlation of Planet images. Our observations show that the glacier snout has been progressively advancing in recent four decades, with a stepwise increase of advance velocity from 4.25 ± 0.28 m·a^{-1} between 1975 and 2009 to 32.53 ± 4.45 m·a^{-1} between 2015 and 2019. DEM differencing confirms the glacial advance, with surface thinning in the source region and thickening in the tongue region. The net volume loss over the glacier tongue was about $11.21\pm2.66 \times10^5$ m^3 during 1975–2019. Image cross-correlation reveals that

25 the surface flow velocity of the glacier tongue has been increasing in recent years, with the mean velocity below 4800 m almost trebled from 22 ± 4 cm·a^{-1} during 2009–2012 to 61 ± 5 cm·a^{-1} during 2016–2019. Piecing these observations together, we suggest that the flow of the glacier tongue is mainly controlled by the geometry of the glacier, while the presence of an ice-dammed lake and a supraglacial pond implies a hydrological influence as well. Taking the glacier tongue as an avalanche source, we quantitively simulated the potential runout distance using the Voellmy-Salm avalanche model. The simulations predict that the

30 avalanche of the glacier tongue will result in a maximum runout distance of about 1.3 km with moderate friction parameters, unlikely to threaten the safety of the Qinghai-Tibet railway.

Natural Hazards
and Earth System
Sciences
Discussions
EGU
Open Access

1. Introduction

Glacier instabilities in the form of ice break-offs and avalanches are universal phenomena (Faillettaz et al., 2015; Haeberli et al., 2004; Jacquemart et al., 2020). Most of the glacier instabilities occur on steep glacier termini or hanging glaciers, while

35 recent studies show that ice detachment can also occur in low-angle (lower than around 20°) valley glaciers (Kääb et al., 2020). The catastrophic collapse of part or even whole of a glacier can transport ice mass downstream to a distance of up to tens of kilometers, with a typical volume in the order of $10^6\,\text{m}^3$. Due to the hazardous threats of glacier collapse to people's lives and infrastructure, distinguishing the collapse-prone glaciers from the non-threatening ones is crucial for hazard mitigation.

Several extraordinary low-angle glacial detachment events have been reported in recent years. One of the earliest events that

40 have been documented in detail is the destructive 2002 Kolka glacier collapse in Russia, which killed about 140 people due to the mass flow (Haeberli et al., 2004; Huggel et al., 2005). Another destructive event raising great attention is the 2016 collapses of two valley glaciers in the Aru mountain range in the western Qinghai-Tibet Plateau (QTP), which caused nine casualties (Bai and He, 2020; Gilbert et al., 2018; Kääb et al., 2018; Tian et al., 2016). In addition to these two well-known events, a few historical collapses of valley glaciers are recently recognized and analyzed, such as the 2007 detachment of Leñas glacier in

45 the Argentinian Andes (Falaschi et al., 2019), the three repeat collapses (in 2004, 2007, and 2016) of a glacier in the Amney Machen mountain range of the eastern QTP (Paul, 2019), and the twice (2013 and 2015) collapses of the lower parts of Flat Creek glacier in Alaska (Jacquemart et al., 2020). Recent research suggests that glacier detachments occur more frequently than previously thought (Kääb et al., 2020).

A wide range of triggers can lead to a glacier detachment. Possible triggering factors include changes in ice thermal regime,

50 morphology of a glacier, and atmospheric conditions. Specifically, increasing air temperatures, coupled with enhanced precipitation, plays an important role in initiating the ice detachment (Gilbert et al., 2018; Tian et al., 2016). Some detachments occurred in surge-type glaciers. For example, the Kolka glacier and the Amney Machen glacier have experienced repeated surging in history (Kotlyakov, 2004; Paul, 2019). The collapses of Aru glaciers were also preceded by geometry changes in the form of surge-like behaviors, although they were not known as surging before (Gilbert et al., 2018; Kääb et al., 2018).

55 Meanwhile, studies have highlighted that sudden detachments can occur on glaciers with no historical records of instability (Kääb et al., 2018; 2020).

Recent glacier collapse events on the QTP have raised concerns on the stability of glaciers there, especially under intense climate warming. In recent decades, air temperatures recorded by weather stations on the QTP have been increasing at a mean rate of 0.3~0.4 °C·10a^{-1}, which is twice the global mean rate (Chen et al., 2015). While previous studies of glacier instabilities

60 in QTP mainly focus on the Karakorum and West Kunlun mountain regions where a large number of surge-type glaciers exist (Bhambri et al., 2020; Leinss et al., 2019; Yasuda and Furuya, 2015), little is known about glacier instabilities in the inner region of the plateau. Considering that large-volume ice detachments can occur on low-angle mountain glaciers, it is essential to investigate the long-term dynamics of glaciers prone to collapses and further assess their potential impacts.

65 In this study, we present a comprehensive analysis of the dynamics of a small low-angle valley glacier (94.145°E, 37.678°N) in the East Kunlun Mountains of QTP (Fig. 1). We refer to the glacier's name as 'KLP-37' since it is located at the Kunlun Pass (KLP) of the East Kunlun Mountains and numbered 532EB037 in China's second glacier inventory (Guo et al., 2010). We identified the glacier, close to the Qinghai Tibet railway and highway, during a field trip in the KLP region in 2016 (Wang et al., 2020). The presence of intense crevasses on the glacier surface raises the question if a hazardous ice avalanche is imminent.

70 To assess the stability of the KLP-37 glacier, we employed multi-sensor satellite imagery to characterize its morphological changes and dynamics in the recent 40 years. The changes in the terminus position of the glacier were tracked by interpreting optical images from the Planet constellation and Google Earth. We collected/constructed six DEMs over the glacier between 1975 and 2018 to quantify the surface elevation variations. The 1975 DEM was reconstructed using a stereo image pair from the Hexagon KH-9 reconnaissance satellite. The surface velocities of the glacier tongue from 2009 to 2019 were also mapped

75 using image cross-correlation. Combining the decadal geomorphic changes and surface velocities, we discussed the possible mechanisms accounting for the dynamics of the KLP-37 glacier and estimated the potential runout distance if a failure of the glacier tongue occurs in the future. We also discussed how the site-specific study on the KLP-37 glacier could provide new insights into the glacier collapse hazard monitoring and assessment.

2. Study site and remote sensing data

80 ### 2.1 Study site

The KLP is located in the central part of the East Kunlun Mountains in the inner QTP (Fig. 1a). The KLP region is also tectonically active. The Kunlun fault, one of the principal left-lateral strike-slip fault systems in the northern part of the QTP, runs for about 1600 km along the west-east and splays into two sub-fault segments at the KLP (Fig. 1a). The Kunlun fault system generated a few Mw>7 earthquakes in the last 100 years, including the most recent two in 2001 (Mw7.8) and 1963

85 (Mw7.1) (Lasserre et al., 2005). Notably, the 2001 event, with its epicenter only ~45 km west of the KLP-37 glacier (Fig. 1a), induced several ice avalanche events (see the yellow dots in Fig. 1a) over the glaciers in the KLP region (Jerome et al., 2004).

The KLP-37 glacier rests on the northern slope of the East Kunlun Mountains. The glacier terminates about 3 km from the Qinghai-Tibet railway and highway, which crosses the Xidatan basin along the west-east direction (Fig. 1b). The Xidatan basin is also the northern permafrost boundary of the QTP (Wu et al., 2005). The climate is typically cold and arid: the annual mean

90 air temperature is -2.9 ºC, and the average annual precipitation is about 400 mm, with most of the precipitation concentrating in summer from May to September (Luo et al., 2018). The snow line in this region is about 4960 m above sea level (Yue et al., 2013). The lithology on the slope where the KLP-37 glacier lays mainly consists of Triassic metamorphic sandstone and sand slate, with typical grain diameters of 2–5 cm (Wu et al., 1982). The rock fragments are strongly weathered and filled with fine-grained (pelitic to sandy) sediments (Wu et al., 1982), suggesting the KLP-37 glacier likely rests on a soft bed.
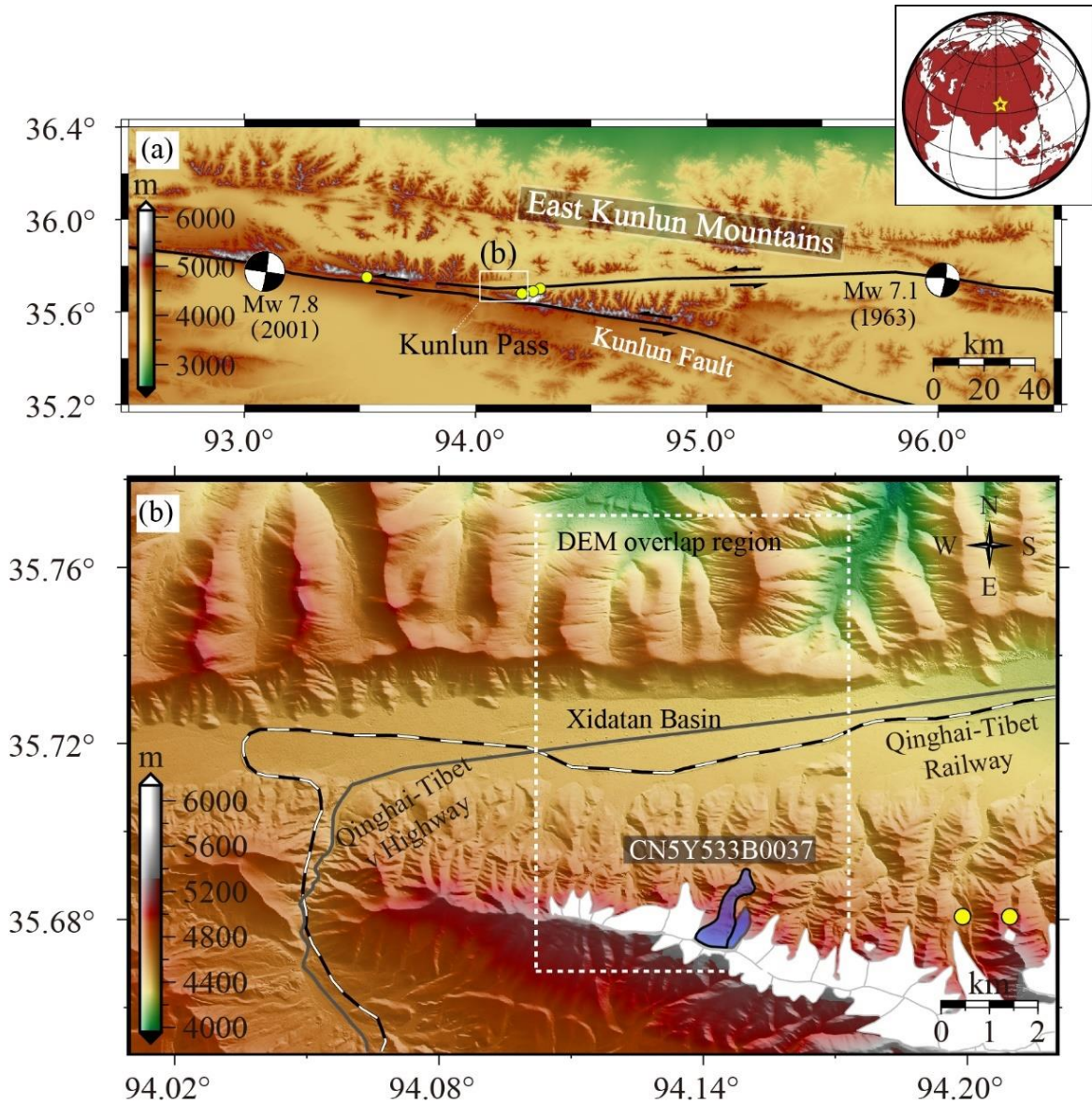
Figure 1: (a) The geological setting of the study area. The black lines depict the Kunlun fault traces. The yellow dots mark the ice avalanche locations induced by the 2001 Mw 7.8 earthquake (Jerome et al., 2004). (b) The topography of the Kunlun Pass region. The white rectangle shows the overlap region of the DEMs used in this study. The polygons are the glaciers from the GAMDAM glacier inventory (Sakai et al., 2019), while the one filled with purple color is the KLP-37 glacier, whose west branch is outlined in thick black.

The KLP-37 glacier is a small low-angle valley glacier consisting of two branches (the GAMDAM glacier inventory, Sakai, 2019). Here our analyses mainly focus on the west branch, which has a length of about 2.06 km and a mean slope of about 20°.

The elevation range of the glacier spans between 4650 and 5450 m. Particularly, compared to the east branch of the glacier,
the west branch's snout terminates at an elevation lower than about 220 m (Fig. 2a), leading to a hypothesis that a pre-collapse

105 event may have occurred there before. The width of the glacier gradually narrows from the accumulation zone to the
downstream. From the satellite image taken in the summer of 2013 (Fig. 2a), we can observe an ice-dammed glacier lake east
of the tongue region and a supraglacial pond on the tongue surface. The field photo on 27 June 2016 exhibits multiple
horizontally distributed fissures at the glacier accumulation area (Fig. 2b). We can also observe fine debris covering the glacier
tongue and alluvial fans in the forefield from the high-resolution Google Earth image and field photos (Fig. 2), supporting the

110 hypothesis that the glacier lays on a weak bedrock. The developed crevasses, exposed ice cliffs, and glacier ice are also clearly
visible in the tongue region, indicating the tongue is highly active (Fig. 2c).
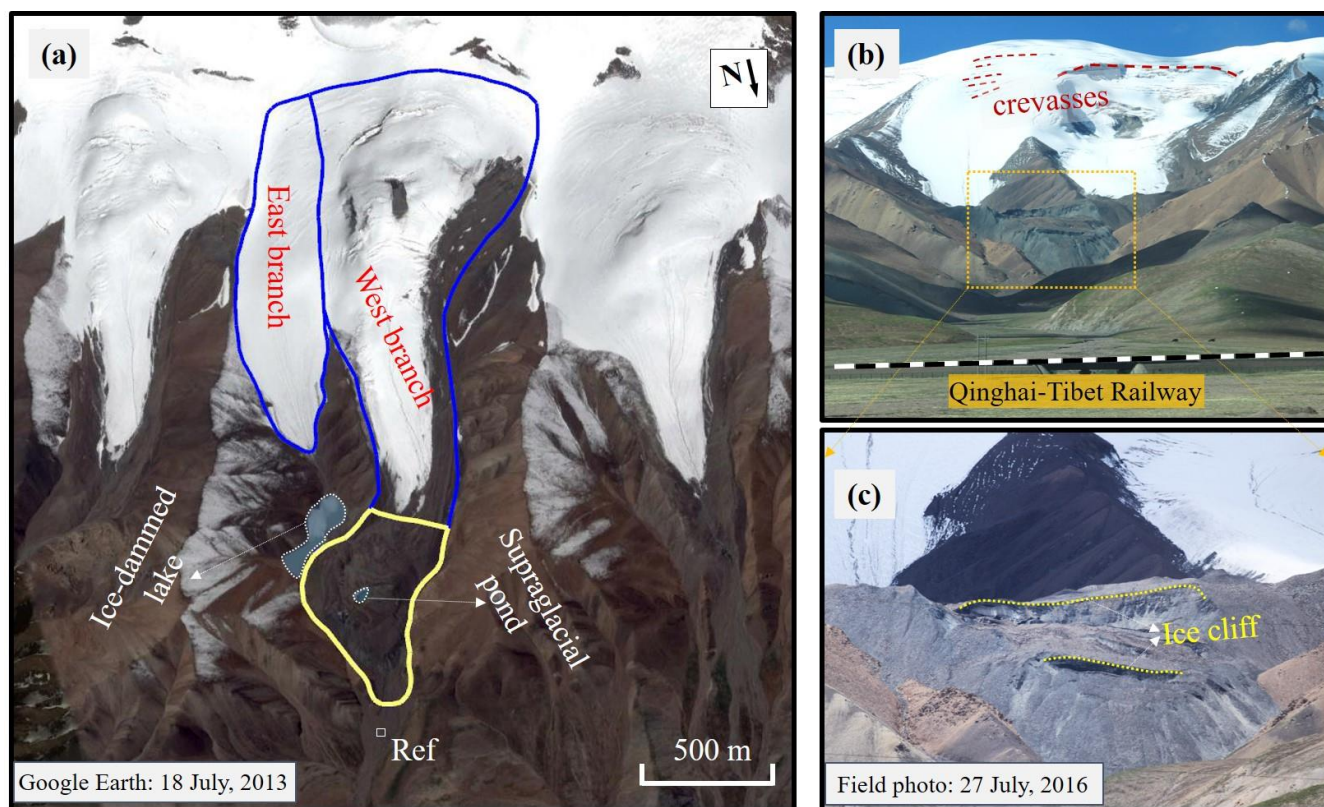
Figure 2: (a) The outline of the KLP-37 glacier overlapped on a Google Earth image of 18 July 2013 (© Google Earth™).
An ice-dammed glacier lake and a supraglacial pond are also depicted. (b) and (c) are the field photos acquired by the

115 author on 27 July 2016, which exhibits the crevasses and ice cliffs on the glacier surface. The rectangle annotated with
"Ref" in (a) indicates the area for estimating image cross-correlation error (see Section 3.3).

2.2 Remote sensing data

Table 1 lists the satellite remote sensing data used in this study. The data types include optical orthoimages, stereo images, and multiple DEMs derived from both stereo-photogrammetry and SAR interferometry. All the data were referenced to the coordinate system of UTM zone 46 N.

Tracking the boundary changes of glaciers is typically based on the freely available Landsat, Sentinel-2, and ASTER satellite images, which commonly have a spatial resolution of about 10 meters (Bolch et al., 2011; Scherler et al., 2011). Considering that KLP-37 is a small valley glacier with a width of only about 200 meters, we collected five RapidEye (5 m spatial resolution) and four PlanetScope (3 m) orthoimages acquired by Planet's constellation of cubesats between 2009 and 2019. All the Planet scenes are ortho products and consist of visible and near-infrared frames. We also used the high-resolution Google Earth image to assist in the boundary delineation and detailed morphology characterization.

We collected a stereo-pair acquired by the Hexagon KH-9 spy satellite in 1975 to reconstruct the topography of the KLP-37 glacier decades ago. The KH-9 images (image IDs: DZB1211-500024L002001 and DZB1211-500024L003001), with a ground resolution of about 7.6 m, were scanned by the U.S. Geological Survey (USGS) at a resolution of 7 mm. The formation procedure of the KH-9 DEM using stereo-photogrammetry will be detailed in Section 3.2.1. We also generated the orthorectified KH-9 images, from which the glacier boundary was further identified.

In addition to the KH-9 DEM, we collected another five DEMs in different periods between 2000 and 2018 to infer the elevation changes of the KLP-37 glacier after 1975. Of the five DEMs, three were obtained from optical stereo-image photogrammetry, and the other two were generated using SAR interferometry. The latest DEM (2018) was generated from an ASTER stereo-image pair acquired by the Terra satellite (Hirano et al., 2003). Two 8-meter High Mountain Asia (HMA) DEMs (2010 and 2014) were generated from very-high-resolution imagery from Worldview-1/2 satellites by Shean (2017). The SAR interferometry derived DEMs include the freely available SRTM (2000) and commercial TanDEM, with spatial resolutions of 30 m and 12 m, respectively (Farr et al., 2007; Krieger et al., 2007). Two kinds of SRTM DEM data exist, which are generated from radar data with different wavelengths (i.e., C-band and X-band). Here both the C- and X-band SRTM DEMs were used to correct for the penetration depth of radar wavelength. The commercial TanDEM was produced from the TerrSAR-X/TanDEM-X SAR images acquired between January 2011 and September 2014, representing an average estimate over the period. We, therefore, did not use the TanDEM to calculate elevation changes of the glacier surface. Instead, the TanDEM was taken as a reference to evaluate the accuracy of the other DEMs because of its relatively high vertical accuracy (~2 m) (Riegler et al., 2015). The TanDEM was also used to extract the elevations of the selected ground control points (GCPs) when constructing DEM with the ASTER stereo-images (see Section 3.2.1).

3. Methodology

3.1 Derivation of glacier terminus changes

We manually digitized the boundary of the glacier from the orthorectified KH-9 image and the nine Planet orthoimages. The

150 boundaries of the snow-covered part of the KLP-37 glacier were cross-checked against the GAMDAM glacier inventory (Sakai, 2019). We identified the center point of the glacier terminus in each image and then estimated the advance distance between two consecutive periods. To avoid the influence of spatial resolution on the determination of the terminus center point, all the images were resampled into a common geometry with a spatial resolution of 3 m, the same as the resolution of the PlanetScope images. By dividing the advance distance by each image pair's time span, we further estimated the terminus advance velocities (v_t) during 1975 and 2019. The uncertainty of the velocity estimate can be written as (Hall et al., 2003; Rashid et al., 2020)

155
$$\varepsilon_{v_\text{t}} = (\sqrt{r_1{}^2 + r_2{}^2} + \varepsilon_\text{geo})/\Delta t \tag{1}$$

where r_1 and r_2 are spatial resolutions of the two images, respectively; ε_geo is the relative georeferencing error between the two images, which is set to be zero because all the optical images used are orthorectified and georeferenced products.

3.2 Surface elevation changes from DEM differencing

3.2.1 DEM extraction from stereo images

160 We used the HEXIMAP toolbox, developed by Maurer et al. (2016) and coded in MATLAB with an automated pipeline, to extract DEM with the KH-9 stereo images. HEXIMAP combines computer-vision concepts with traditional photogrammetric methods to achieve a satisfactory solution of DEM accuracy. The OpenCV library is used in HEXIMAP for surface feature matching, uncalibrated stereo rectification, and semiglobal block matching. Each digital KH-9 image provided by the USGS consists of two sub-frames with some overlap. The preprocessing steps thus include the stitching of sub-frames and cropping

165 to the region of interest. Because the exterior parameters of KH-9 images are unavailable, HEXIMAP first generates a DEM with only rough geographical coordinates and then refines the DEM by matching it to an external reference DEM (Maurer et al., 2016). Here we used the TanDEM as the reference DEM and finally extracted the KH-9 DEM with a spatial resolution of 15 m. Fig. S1 (see the Supplementary file) shows the generated KH-9 DEM for the study area.

We used the open-source ASP (Ames Stereo Pipeline, v2.6.2) software developed by NASA to extract DEMs based on the

170 ASTER stereo images. The ASP software provides a program called "aster2asp", which implements a straightforward pipeline for processing ASTER stereo images and extracting DEM (Shean et al., 2016). To ensure the DEM accuracy, we selected 12 GCPs on the high-resolution Planet image (2016/10/10) and determined the elevations of GCPs with the TanDEM data. The ASTER DEM was also generated with a spatial resolution of 15 m.

3.2.2 DEM co-registration and differencing

175 With the KH-9 (1975), SRTM (2000), HMA (2010 and 2014), and ASTER (2018) DEMs, we formed four pairs with consecutive times to perform DEM differencing. All the DEMs were resampled into the overlap region shown in Fig. 1b (see the white box) with a spatial post of 15 m. The DEM pairs needs to be co-registered to minimize the errors associated with geometric shifts. We used the method that relies on the geometric relationship between the shift vectors and the slope and

terrain aspect to coregister the DEM pairs (Nuth and Kääb, 2011). The co-registration follows the principle that the DEM

180   differences (Δh) can be expressed as a function of slope (α) and aspect (φ)

$$\frac{\Delta h}{\tan(\alpha)} = a \cdot \cos(b - \varphi) + c \qquad (2)$$

where a, b, and c are the unknown model parameters, which can be determined using the DEM difference values over stable off-glacier regions. The glacierized regions and the area with a slope smaller than 10° were excluded before the coregistration. After the co-registration, the older DEM of a pair was then resampled using the cubic interpolation method with a resampling

185   post of 15 m. Elevation differences were calculated by subtracting the older DEM from the younger DEM such that glacier thickening values are positive. Fig. 3 shows an example of DEM differences before and after the co-registration with the two HMA DEMs (see Table 1), demonstrateing a remarkable reduction of residuals due to geometric shifts between DEMs. We also calculated volume changes over the glacier tongue area (the yellow polygon in Fig. 2a) during different periods based on the elevation change estimates.
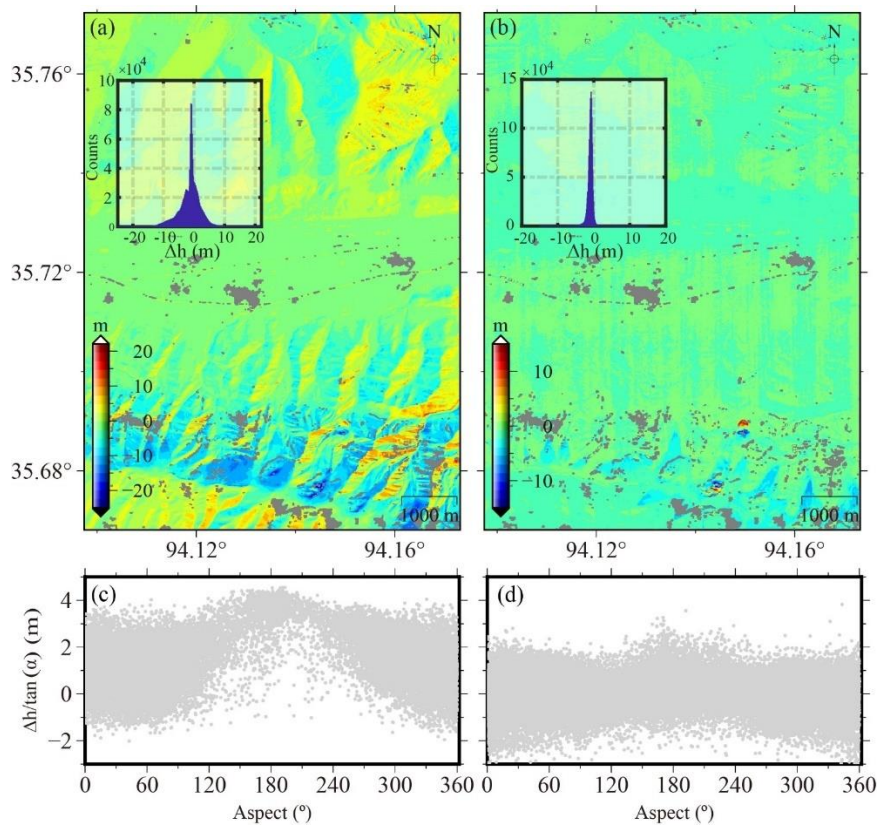
190

Figure 3: Comparison of DEM differences before (a) and after (b) coregistration. The inset histograms exhibit distributions of DEM differences. (c) and (d) exhibit the plots of $\Delta h / \tan(\alpha)$ against aspect angle before and after the co-registration. Note α represents the slope angle.

Two possible systematic biases resulted from (1) the penetration of radar wave and (2) the seasonal snow cover on the glacier
should be corrected in DEM differencing. We used the SRTM-C DEM to calculate elevation changes between 1975/12/12–
2000/02 and 2000/02–2104/10/18, while the C-band radar wave can penetrate several meters into ice. Considering the low
penetration depth of X-band radar into snow/ice surface, we used the X-band SRTM DEM (SRTM-X) as a reference to correct
for the bias of the SRTM-C DEM. The elevation differences over the KLP-37 glacier between the X- and C-band SRTM DEMs
were calculated, from which we found that the elevation differences below 5200 m are nearly constant with a mean of
2.82±0.86 m, similar to the previous estimates ranging from 1.9 to 3.1 m (Kääb et al., 2012; Gardelle et al., 2013, Li et al.,
2017). The offsets increase significantly when elevation is higher than 5200 m. Although the penetration depth varies with the
changes of elevation, we subtracted the constant offset (2.82 m) from the SRTM-C DEM to correct for the penetration depth
because we mainly focus on the elevation change over the glacier tongue region in this study. Snow cover changes due to the
different acquisition times of DEMs may also contribute to the estimate of glacier elevation change (Gardelle et al., 2013).
This effect is usually referred to as the seasonality artifacts in DEM differencing. All the DEMs we collected were acquired
during winter except for the HMA DEM of late August in 2014. We did not apply adjustments to winter-winter DEM pairs
because KLP-37 is a summer-accumulation type glacier. However, elevation changes for the summer-winter DEM pairs (i.e.,
HMA10-HMA14 and HMA14-ASTER) need to be corrected by considering four to five months of time differences. Similar
to the previous studies (Li et al., 2017), we conservatively adjusted the HMA DEM in 2014 by applying an empirical bias
correction of 0.1 m per month due to the scarcity of snow depth documentation around the glacier.

3.2.3 Uncertainty assessment

Elevation change uncertainty estimates were calculated based on off-glacier elevation changes in the DEMs' overlap region
(see the white rectangle in Fig. 1b). We calculated the uncertainty statistically by dividing the altitude into different bands with
a 50 m interval. We assumed that the error for each pixel of elevation change ($\varepsilon_{\Delta h}^i$) is equal to the standard deviation of the
mean elevation change of its elevation band, which can be calculated according to standard principles of error propagation
(Gardelle et al., 2013)

$$\varepsilon_{\Delta h}^i = \frac{\sigma_{\Delta h}^i}{\sqrt{N_{eff}}} \; , \tag{3}$$

where $\sigma_{\Delta h}^i$ is the standard deviation of the elevation changes in the i_{th} elevation band; N_{eff} represents the number of
independent values in the band, which can be calculated as

$$N_{eff} = \frac{N_{tot} \cdot P_s}{2 \cdot d} \; , \tag{4}$$

where P_s is the pixel posting of the DEM; N_{tot} is the total number of elevation change measurements in the elevation band;
d is the distance of spatial autocorrelation of the elevation change maps, which can be obtained by a least-square fit to the
experimental, isotropic variogram of all off-glacier elevation differences. The autocorrelation distances for the four DEM pairs
were 286 m (KH-9–SRTM), 167 m (SRTM–HMA10), 189 m (HMA10-HMA14), and 909 m (HMA14-ASTER), respectively,

Natural Hazards
and Earth System
Sciences
Discussions

225 with a mean value of about 388 m, similar to the typical value of about 500 m by previous studies (McNabb et al., 2019). The error of the glacier volume change ($\varepsilon_{\Delta V}$) was derived from the uncertainty of elevation change:

$$\varepsilon_{\Delta V} = \sqrt{\sum(A_i \cdot \sigma_{\Delta h}^i)^2} \quad , \tag{5}$$

where A_i is the area of each elevation band.

3.3 Surface velocity from image cross-correlation

230 To investigate the dynamics of the KLP-37 glacier tongue, we applied cross-correlation to the orthorectified Planet images to obtain two-dimensional surface displacements. Three image pairs (2009/08/30–2012/09/12, 2012/09/12–2016/09/10, and 2016/09/10–2019/08/06) were formed and correlated for obtaining surface velocities during each period. The acquisition 2015/10/12 was not used because the image is partially affected by snow cover. We extracted the near-infrared band of the Planet images, i.e., the sub-band that has the longest wavelength, to implement the correlation measurement. This is because

235 the long-wavelength band is generally less affected by cloud and has a higher radiometric magnitude.

The freely available, open-source Micmac software was used to implement the sub-pixel image cross-correction (Rosu et al., 2015; Rupnik et al., 2017). The correlator program "MM2DPosSism" provided in Micmac employs a hierarchical matching scheme using normalized cross-correlation (NCC) with a non-linear cost function to find the most likely match for each pixel. The matching cost function is evaluated from the NCC coefficient considering only correlation coefficients $C \geq C_{min}$. Micmac

240 also adopts a unique regularization parameter r to smooth displacement field and reduce noise and outliers, which allows the use of smaller matching template windows targeting small landscape features. Here we set values of 0.5 and 0.3 for C_{min} and r, respectively, and a moving window of 9×9 pixels in the correlation processing. The flow velocity's uncertainties primarily result from the imprecise matching of the surface features on the glacier. Similar to the previous studies (Rupnik et al., 2017), we inferred the uncertainty of flow velocity using the correlation estimate at a stable and plain surface below the glacier

245 terminus (see the white rectangle in Fig. 2a).

4. Results

4.1 Morphological changes and terminus advance

The optical KH-9and Planet satellite images enable us to inspect the morphological changes of the KLP-37 glacier in the recent 44 years. Time-lapses of the optical images covering the full glacier are shown in Fig. S2, and the zooms of the glacier tongue

250 region for a clear inspection are shown in Fig. 4. Satellite images show that the crevasses in the glacier cirque had commenced in the 1975 KH-9 image and became more evident in the following years (see the red arrows in Fig. S2). The snowpack downstream of the crevasses collapsed sometime between 2013/08/04 and 2015/10/12, indicated by the changes of the crevasses' length and width. The highly developed crevasses in the glacier accumulation region since the 1970s indicate that

the glacier had remained unstable for at least four decades. Also, the glacier tongue exhibits a swollen body with a steep front
255 in the KH-9 image (Fig. 4a), indicating a large amount of ice mass had been deposited there by 1975.
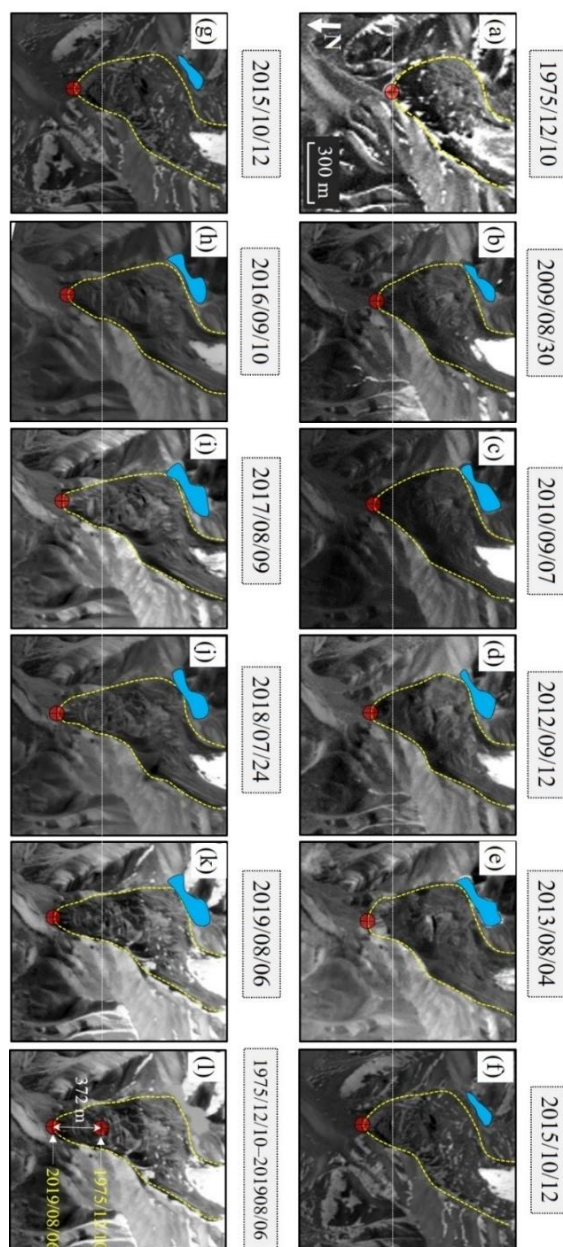

Figure 4: Optical satellite images covering the KLP-37 glacier tongue. (a) Hexagon KH-9 image acquired on 1975/12/10 (© U.S. Geological Survey); (b-k) Planet images acquired during 2009/09/07 and 2019/08/06 (© Planet Labs); (l) Comparison of the glacier terminus position between 2917 and 2019. The horizontal white dotted lines provide a
260 **reference for the terminus position in 1975. The blue polygons represent the ice-dammed glacier lake.**

Satellite optical images also clearly show the evolution of the ice-dammed lake (the light blue polygons in Fig. 4) developing in the front of the glacier's west branch. The lake were not visible in the 1975 image. However, we cannot rule out the possibility that the coarse resolution (~ 7.6 m) of the KH-9 image may hinder the identification of the lake. The high-resolution Google Earth image in 2005 shows that the ice-dammed lake had appeared before then (Fig. S3). To investigate the changes
265   in lake area over time, we delineated the boundary of the lake based on the Planet and Google Earth images and estimated the lake area between 2005 and 2019 (see Table S1). The lake area peaked in summer and decreased in winter. The lake area showed an expansion trend in recent years, with the smallest value (3745 ± 229 m^2) in the winter of 2010 and the largest value (21276 ± 1646 m^2) in the summer of 2017. A small supraglacial pond developed in the depressions on the glacier tongue surface; The pond (Figs. 2a and 4) appeared in 2013 and disappeared in 2017.
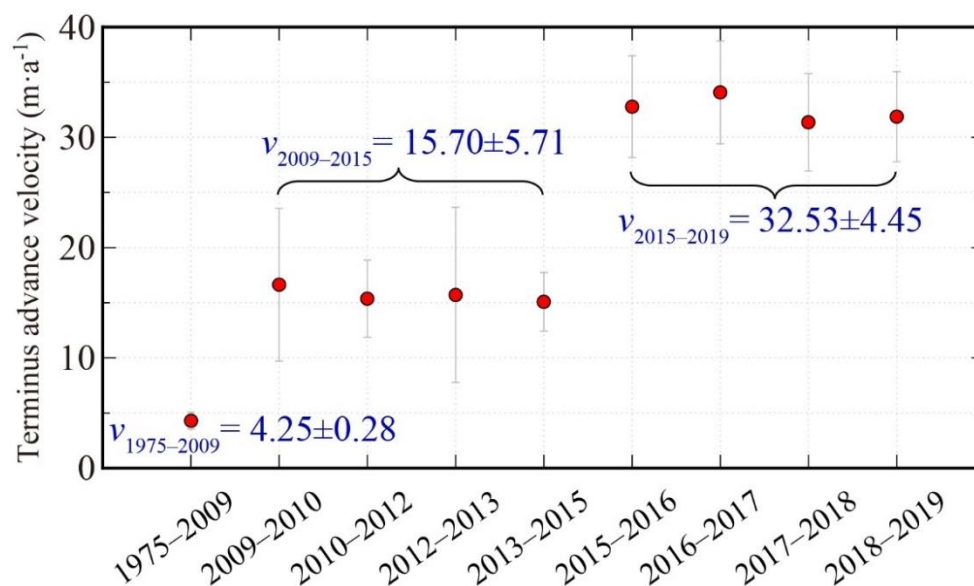
Figure 5: Terminus advance velocities and the associated uncertainties (the light gray error bars) of the KLP-37 glacier estimated from KH-9 and Planet images. We also annotated the mean velocities during three periods: 1975–2009, 2009–2015, and 2015–2019. Note the time axis is not equally posted for a better presentation.

The glacier terminus showed a stepwise advance pattern (see the red points at the glacier snout in Fig. 4) between 1975 and
275   2019. Table S2 lists the terminus point coordinates in each satellite image, and Fig. 5 shows the changes in terminus advance velocities during periods between the consecutive image acquisitions. The glacier tongue moved downstream and narrowed due to the topographic blocking on both sides. The glacier terminus' total advance distance was about 372 ± 17.63 m in recent 40 years (Fig. 4l). The advance velocity between 1975 and 2009 was about 4.25 ± 0.28 m·a^{-1}, while the velocity had been higher than 10 m·a^{-1} after 2009. The velocities were similar during the each period of 2009–2015 and 2015–2019. The mean velocity
280   was 15.70 ± 5.71 m·a^{-1} during 2009–2015 and abruptly increased to 32.53 ± 4.45 m·a^{-1} during 2015–2019.

Natural Hazards
and Earth System
Sciences
Discussions

Open Access

EGU

4.2 Surface elevation and volume changes

We evaluated the accuracies of the DEMs before DEM differencing using the TanDEM as a reference. Most of the elevation differences range between -10 and 10 m (see Fig. S4). The mean values of the off-glacier elevation differences between the TanDEM and other DEMs are all smaller than 0.2 m, indicating that the accuracies of the DEMs we collected are feasible for inferring the elevation changes of the KLP-37 glacier by DEM differencing.
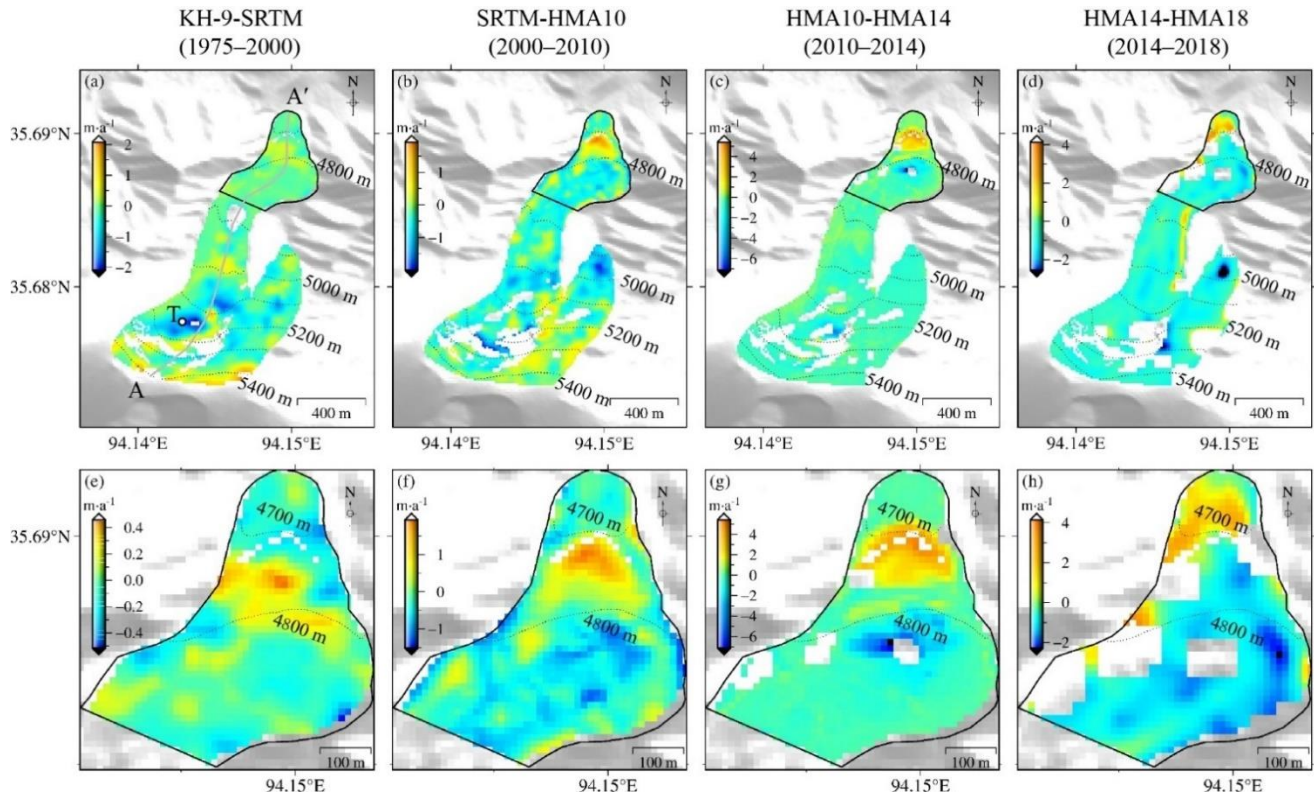
Figure 6: Surface elevation changes of KLP-37 glacier between 1975 and 2018. (a-d) Elevation changes over the full glacier for the DEM pair KH-9-SRTM (1975–2000), SRTM-HMA10 (2000–2010), HMA10-HMA14 (2010–2014), and HMA14-ASTER (2014–2018), respectively. (e-f) Amplified elevation changes over the glacier tongue region for the four DEM pairs. The black dotted lines indicate the elevation contours.
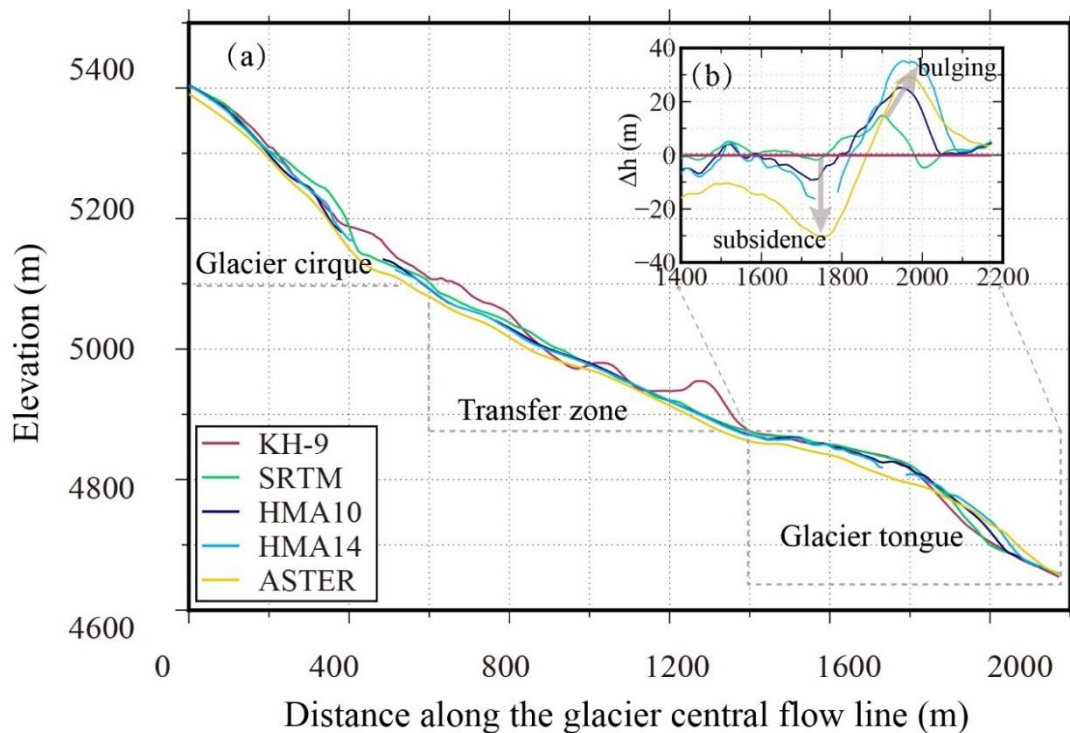
Surface elevation changes of the KLP-37 glacier from DEM differencing overall exhibit thinning in the glacier source region and thickening in the glacier tongue (Fig. 6a-d). The void regions mainly appear in the accumulation area of the glacier's west branch, where the slopes are steep and intense crevasses developed. We selected a specific point ′T′ with a window size of 3×3 pixels (~ 2000 m^2) in the center of the accumulation region (see Fig. 6a) and found that the elevation differences at this point for the KH-9–SRTM, SRTM–HMA10, HMA10–HMA14, and HMA14–ASTER pairs are -1.64±0.77, -0.22±0.15, -0.90±0.31, and -0.02±0.34 m·a^{-1}, respectively. Although the estimate from the HMA14-ASTER DEM pair has considerable

13

uncertainty, the elevation change rate at point ′T′ showed a decreasing trend during 1975–2018. Elevation differences in the east branch of KLP-37 showed a thinning pattern during the recent 40 years, with mean values of -0.18±0.12, -0.32±0.15, -0.48±0.09, and -0.82±0.55 m·a^{-1} for the four DEM pairs, respectively. The continued thinning of the glacier's east branch

300   presumably explains the expansion of the ice-dammed glacier lake, which develops in the front of the east branch and receives the meltwater from the glacier directly.

The elevation changes over the glacier tongue region are enlarged and shown in Fig. 6e-h. We can observe evident elevation increases in the front part of the tongue and distributed thinning just above the bulging area in each elevation change map. Specifically, thinning was prevalent between the elevations of 4750 m and 4880 m for the SRTM–HMA10 and HMA14–

305   ASTER DEM pairs. The snout of the bulging area continually advanced from 1975 to 2018, with a remarkable advance during 2014–2018. Elevation changes confirm the stepwise glacial termini advance (see Section 4.1) and imply a surge-like process in the tongue area in the recent four decades. We calculated the volume changes over the glacier tongue and found that the volume decreases were higher than the increases for all the four DEM pairs (Table 2). The net volume changes calculated from the four DEM pairs were -1.54±1.18, -5.74±1.47, -0.49±0.11, and -3.44±1.87 ×10^5 m^3, respectively, with a total net volume

310   change of -11.21±2.66 ×10^5 m^3, indicating the continued loss of mass over the glacier tongue region.

Figure 7: Glacier surface topography extracted from the five DEMs along the glacier central flow line AA′ (Fig. 6a). The inset shows the elevation changes along the profile with respect to the KH-9 DEM in 1975.

14

Fig. 7 shows the changes of surface topography from 1975 to 2018 along the glacier's central flow line (see AA′ in Fig. 6a).

315 We roughly divided the glacier into three parts: glacier cirque (> 5100 m), transfer zone (4880–5100 m), and the glacier tongue (4700–4880 m). The cirque zone has a mean steep slope angle of about 34°, while the slope becomes gentle in the transfer zone with a mean slope of 19°. Both the glacier cirque and transfer zone exhibited an overall subsidence pattern. The glacier tongue can be further divided into thinning and thickening parts at the elevation of 4780 m. Notably, the thinning rate in the glacier tongue region was much higher than that in the transfer zone (see the subsidence arrow in Fig. 7b). The part above

320 4780 m continually subsided while the lower part bulged, with the peak of bulging moved toward the glacier terminus progressively (Fig. 7b).

Uncertainties associated with the glacier surface elevation changes were evaluated with the statistics of off-glacier elevation differences based on Equation (4). The uncertainties of elevation changes generally increase with elevation (Fig. 8). The mean uncertainties of elevation changes over the glacier tongue region (4700–4880 m) were about 0.04, 0.08, 0.02, and 0.41 $m \cdot a^{-1}$

325 for the KH-9-SRTM, SRTM-HMA10, HMA10-HMA14, and HMA14-ASTER DEM pairs, respectively. Elevation changes in the DEM accumulation region (>5100 m) had relatively higher uncertainties, with mean values of 0.06, 0.06, 0.03, and 0.54 $m \cdot a^{-1}$ for the four DEM pairs.
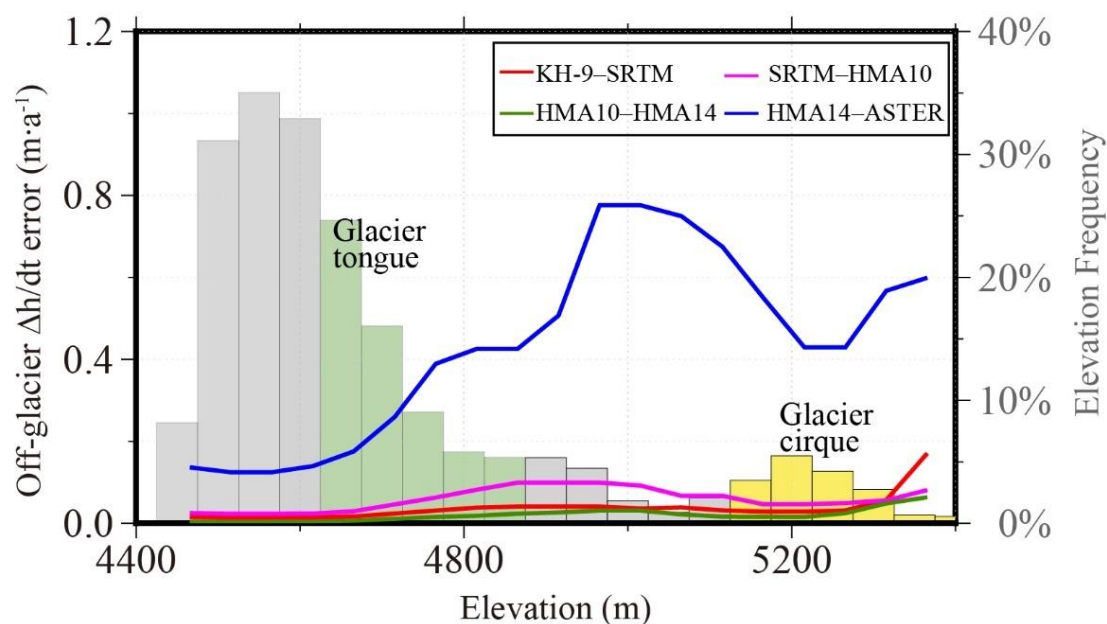

Figure 8: Uncertainty of elevation change estimate as a function of elevation bands (the lines) in the off-glacier region.
330 **The right axis annotates the frequency number of each elevation band. The elevation bands with green and yellow colors represent the glacier tongue and cirque ranges, respectively.**

4.3 Surface flow velocities

Surface flow velocities of the KLP-37 glacier tongue from the cross-correlation of Planet images exhibited an acceleration pattern during 2009/08/30–2019/08/06 (Fig. 9). The maximum velocities were about 92±8, 63±7, and 151±12 cm·a^{-1} for the periods 2009–2012, 2012–2016, and 2016–2019, respectively. We found that the velocity field showed different patterns below and above 4800 m, where the glacier flow direction changed. The velocities in the upper part were heterogeneously distributed, while the velocities below showed a relatively even distribution pattern. Moreover, the velocities in the upper part were generally higher than the lower part. Comparisons between the velocities and topography variations along the central profile PP′ (Fig. 10) indicate that the flow velocities were not correlated with elevation and slope. The velocities below 4800 m were comparable during the periods 2009–2012 and 2012–2016, with mean velocities of 22±4 and 21±2 cm·a^{-1}, respectively; while the mean velocity increased to 61±5 cm·a^{-1} during 2016–2019. The almost trebled mean velocity below 4800 m in the recent decade suggests that the glacier tongue has been getting more active towards an unstable status.
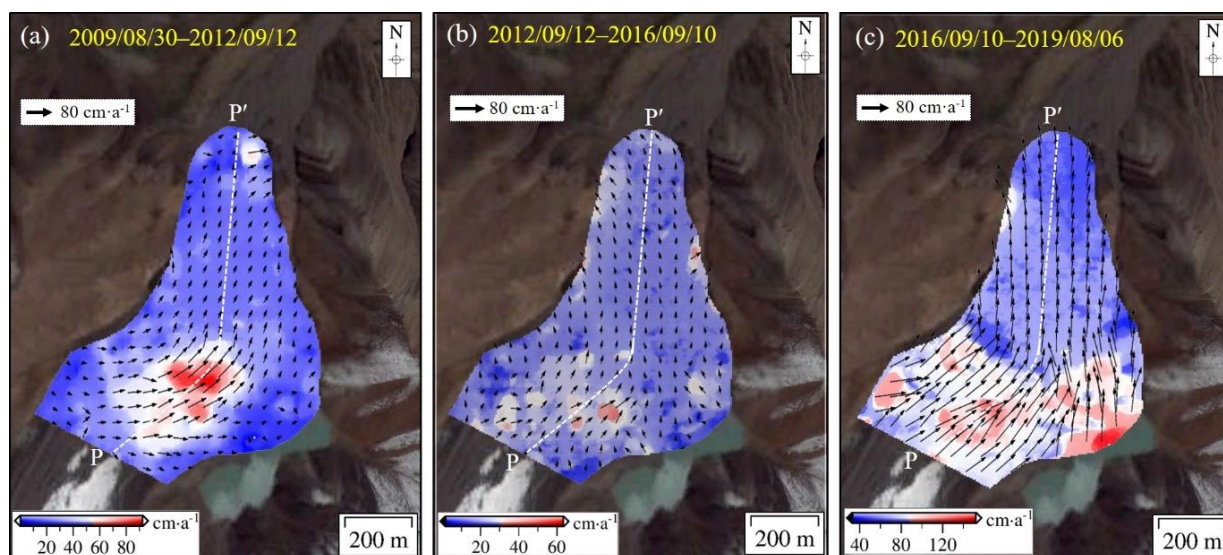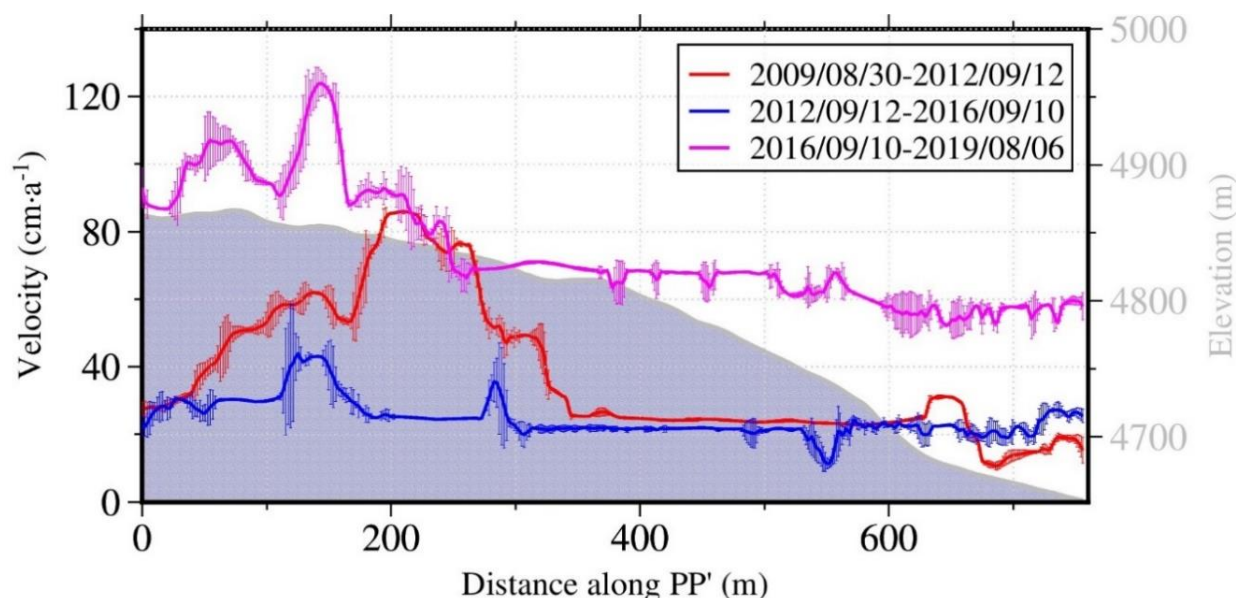

Figure 9: Surface velocities of the glacier tongue of the KLP-37 glacier from image cross-correlation based on the three Planet image pairs (a) 2009/08/30–2012/09/12, (b) 2012/09/12–2016/09/10, and (c) 2016/09/12–2019/08/06. The profile PP′ represents the central flow line, and the arrows mark the flow direction. Note that the colorbar ranges are different. Basemap: Courtesy of © Google Earth™.

The increase in flow velocity after 2016 is consistent with the acceleration of the glacier terminus advance, as detailed in Section 4.1. However, the surface flow velocity measured from image correlation was much lower than the terminus advance velocity. This is probably because (1) the advance of the glacier snout didnot not couple with the whole glacier tongue, and the snout terminus moved faster as a result of the significantly local elevation thinning in the steep front, where the slope

becomes gentle (see Section 4.2). (2) the flow velocities from image cross-correlation represent a local average due to the use of template-based image matching, which may underestimate the true flow velocity of the glacier tongue.

Figure 10: Surface velocities along the glacier central flow line PP′ (see Fig. 9) during the three periods 2009/08/30–2012/09/12, 2012/09/12–2016/09/10, and 2016/09/12–2019/08/06. The light-blue-shaded area indicates the surface topography (right axis) along the profile.

5. Discussion

5.1 Mechanisms of the glacier dynamics

Multi-temporal satellite imagery revealed that the glacier tongue of KLP-37 had been progressively advancing between 1975 and 2019, and the snout advance velocity was accelerating after 2015. From the analysis of changes in surface elevation and temporal flow velocities, we suggest that the KLP-37 glacier tongue was undergoing a slow surge-like process during the observation period. We did not observe this process on the adjacent glaciers, indicating that the KLP-37 glacier has a unique glaciation setting causing the glacier tongue area to be highly active. Previous studies have shown that the factors resulting in glacier acceleration and even collapse mainly include the hydrothermal conditions of glacier basement, topography, and the climate (precipitation/temperature) changes (Jacquemart et al., 2020; Kääb et al., 2020; Kääb et al., 2018; Leinss et al., 2019). Next, we will discuss the possible mechanisms accounting for the dynamics of the KLP-37 glacier tongue.

The thermal regime of a glacier fundamentally influences its dynamics (Leinss et al., 2019). We cannot determine whether the ice/bed interface is temperate because no temperature measurements beneath the KLP-37 glacier are available. Field investigations have shown that the lower permafrost altitude limit of the study region is about 4300 m, lower than the glacier

termini, indicating that the glacier is located in a permafrost environment (Wu et al., 2005). The long preservation of the ice-dammed lake aside from the glacier tongue suggests that the glacier front is probably frozen to the underlying bedrock. This kind of thermal structure for glacier margins and fronts has been found at the collapsed glaciers such as the Aru glacier and the Leñas glacier (Falaschi et al., 2019; Kääb et al., 2018). The frozen base creates a favourable environment for ice

375   accumulation and stress build-up, although it also increases the basal friction which is the threshold to be overcome for detachment occurrence. Detachment or acceleration of the glacier tongue occurs when the force balance cannot be achieved due to the increasing driving stress. Meanwhile, water from the glacial lake may penetrate through fractures and crevasses into the shear sliding interface, leading to the decrease of basal friction and thus accelerating the movement of the glacier tongue. Therefore, we inferred that the ice-dammed lake exerts a hydrological influence on the dynamics of the KLP-37 glacier tongue.

380   The KLP-37 glacier's geometry presumably plays an important role in accounting for the slow surge-like behavior of the glacier. From the high-resolution optical images (Fig. 3), we can observe that the flow direction of the glacier changes from NE24º to NE5º at an elevation of about 4800 m due to the local topography. The glacier tongue downslope of this turning exhibits a "V" shape (the upper part is wide, while the lower part is narrow). The eastward turning and the glacier front's narrowing result in a slowdown of the glacier flow velocity (Fig. 10). Large glacier masses accumulate at the deflection region,

385   thus increasing compressive pressure. Compared with the glaciers nearby, the local topography at the KLP-37 front provides a preconditioning factor for the unstable status of the glacier tongue.
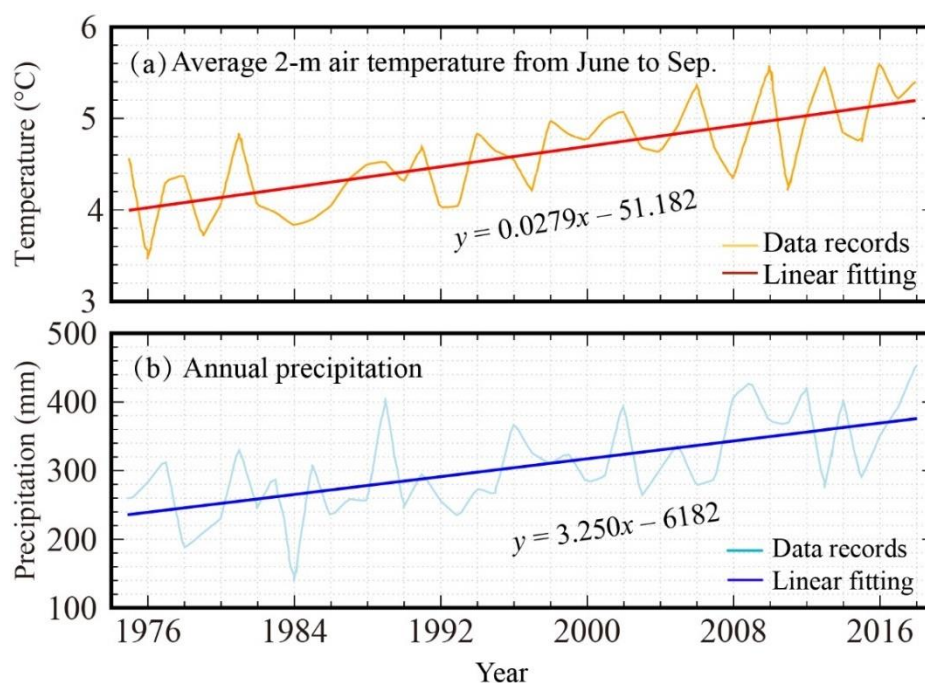
Figure 11: Average 2 m air temperature from June to September (a) and annual precipitation at the Wudaoliang meteorological station about 60 km south of the KLP-37 glacier. The equations annotated represent the best linear

Natural Hazards
and Earth System
Sciences
Discussions

fitting model of the data records.

The trend of a warmer and wetter climate in the recent decades on the QTP may be the long-term driving factor for the continuous advance of the glacier tongue of KLP-37. Fig. 11 shows the mean 2 m air temperature in summer (from July to September) and mean annual precipitation at the Wudaoliang meteorological station about 60 km west (35.3°N, 93.6°E) to the glacier between 1975 and 2018. Both the air temperature and precipitation records show increasing trends: the increase rate of average summer temperature is 0.0279 °C·a⁻¹, while the precipitation has an increasing rate of about 3.250 mm·a⁻¹. The high temperature and precipitation amount during 2015–2018 are likely responsible for the accelerating of the glacier's flow velocity between 2015 and 2019. The expansion of the ice-dammed lake in the recent decade (Section 4.1) also justifies the study area's warming and wetting trend.

Previous studies have revealed that climate warming and increased rainfall can promote glacier movement and eventually lead to glacier collapses (Bai and He, 2020; Kääb et al., 2018; Tian et al., 2016). Taking the Aru glacier as an example, the regional climate warming is likely the reason for changing the glacier from retreat to slow advance in 2013 (a total advance of about 300 m before the ice collapse in 2016) (Tian et al., 2016). Specifically, dense precipitation accounting for 88% of the total precipitation of 2016 has been recorded within 40 days before the Aru glacier collapse, and the extreme precipitation was suggested to be the triggering factor for the glacier collapse (Tian et al., 2016). The increase of meltwater in summer caused by climate warming could increase the overload of glacier surface and the supply of liquid water into the sliding surface, thus further promoting the downward movement of the glacier (Leinss et al., 2019).

In summary, we suggest that the cold glacier front, the particular local topography, and the long-term climate change in the East Kunlun Mountains are the main factors controlling the dynamics of the KLP-37 glacier tongue. With the warming and wetting trend of the local climate, the risk of collapse of the KLP-37 glacier tongue may threaten the safety of the nearby Qinghai-Tibet railway and highway.

5.2 Hazard assessment for the glacier tongue collapse

The KLP-37 glacier shares several similarities with the Aru Glacier. First, both the glaciers exhibited continuous thinning in the source regions and thickening in the tongue regions. Second, the ice flow directions at both the glacier tongues have changed due to the local topography. Also, both glaciers' widths have gradually narrowed down from the source region to the tongue, thus resulting in a large amount of accumulated gravitational potential energy at the glacier front. Although the accumulated volume at the ice tongue of KLP-37 is smaller than that of Aru, the front of the KLP-37 glacier is still at risk of collapse due to its topographic and hydrological conditions.

To quantitively assess the impact of the KLP-37 glacier tongue collapse, we estimated the extent of hazard-prone areas using avalanche-dynamics modeling. We employed the Voellmy-Salm (VS) model to simulate the possible runout distance and flow height of ice materials on the KLP-37 glacier. The VS model was originally developed to investigate the detailed flow patterns

Natural Hazards
and Earth System
Sciences
Discussions

Open Access

EGU

and dynamics related to pure snow valances (Bartelt et al., 1999), while the model has also been widely used to simulate the runout distance of glacier/ice avalanche events (Allen et al., 2009; Bai and He, 2020; Evans et al., 2009).
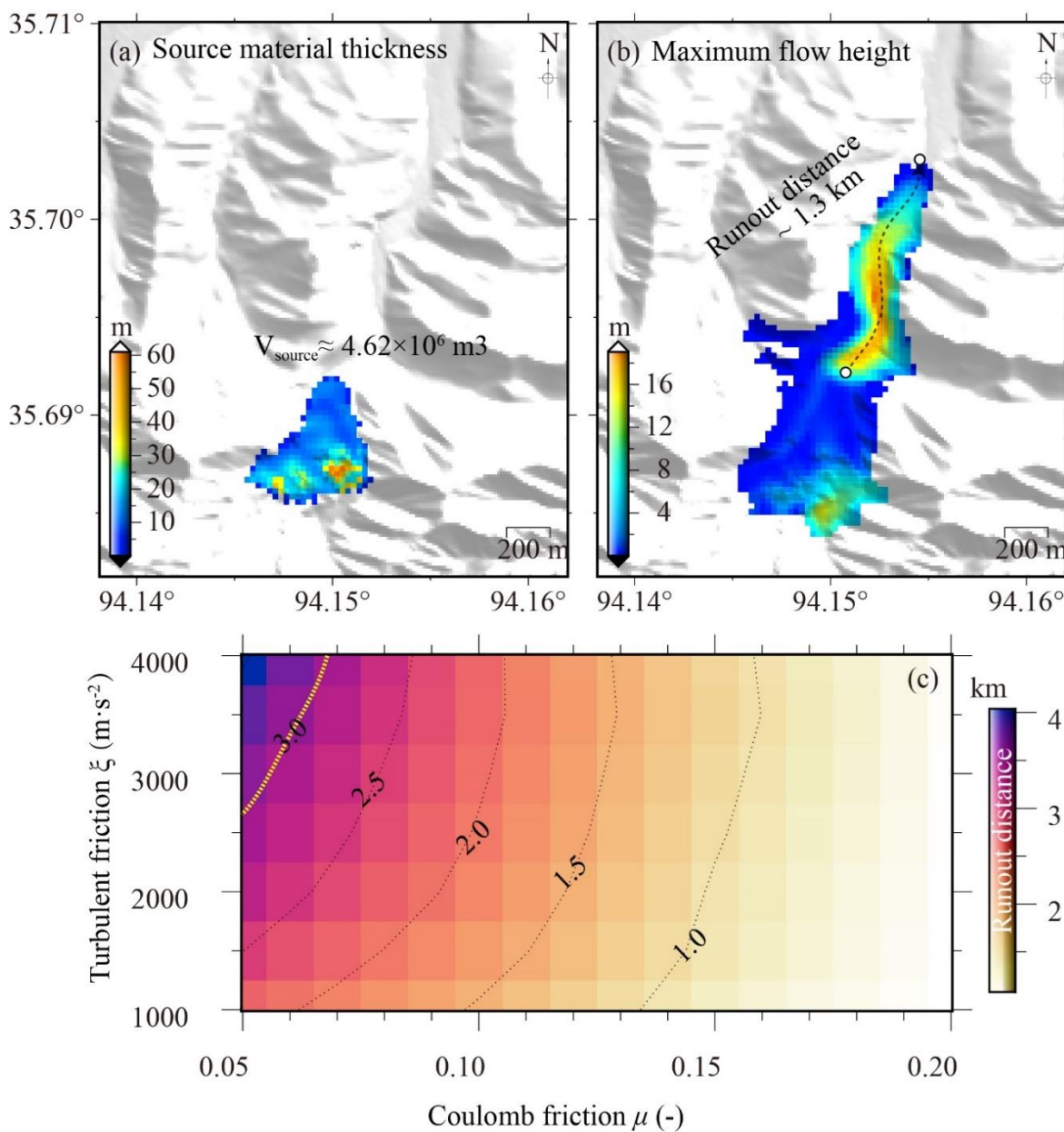

Figure 12: Runout distance estimate for the collapse of the KLP-37 glacier tongue. (a) The thickness of the ice tongue (i.e., avalanche source) derived from the mean surface flow velocity between 2016 and 2019. (b) The simulated maximum flow height of the collapse when choosing moderate friction values of 0.15 for Coulomb friction (µ) and 2500 m·s⁻² for turbulent friction (ξ) in the Voellmy-Salm model. (c) Variations in runout distance for varying µ and ξ.

20

We used the open-source software MASSFLOW to implement the modeling (Ouyang et al., 2013). MASSFLOW contains the VS model and allows for the simulation of rapid mass movements accounting for momentum and including processes of friction, fluidization, and erosion. The input datasets consist of a DEM for generating a meshed grid and a source file containing the geographical extent and thickness of the avalanche materials. Here we used the 7-meter HMA DEM acquired in 2014 as the input topography. The ice thickness was approximately inverted using Glen's flow law based on flow velocities of the KLP-37 glacier between 2016 and 2019 (Glen, 1955; Lambrecht et al., 2014; Wendt et al., 2017). Given the homogenous flow pattern of the glacier tongue as presented in Section 4.3, we assumed that the surface velocity we observed entirely resulted from the internal ice creep. Then, ice thickness can be derived from the surface slope α and the deformation velocity v (Huss and Farinotti, 2012):

$$H = \left(\frac{n+1}{2A(f\rho g)^n}\right)^{1/(n+1)} \left(\frac{v}{\sin(\alpha)}\right)^{1/(n+1)} , \qquad (6)$$

where A and n are the parameters of Glen's flow law for creeping ice, ρ represents the density of ice (900 kg·m⁻³), and g is the gravitational acceleration (9.8 m·s⁻²), f is a shape factor accounting for lateral drag along glacier margins (Huss and Farinotti, 2012). The values for the parameters A, n, and f were empirically set to be 2.4×10⁻²⁴ Pa⁻³·s⁻¹, 3, and 0.9, respectively, same as the modeling settings of cold-based mountain glaciers (Murray et al., 2003). Fig. 12a shows the ice thickness map derived from Glen's flow model. The maximum ice thickness is close to 60 m, and most of the tongue area has ice thickness less than 30 m. Integrating the ice thickness over the entire area indicates a source volume of about 4.62×10⁶ m³. Note the calculated ice thickness and volume probably represent conservative estimates because the input flow velocities from Planet image cross-correlation may underestimate the glacier tongue's true flow rates (see Section 4.3).

The VS model divides avalanche flow resistance into a speed independent Coulomb-type friction (friction coefficient μ) and a velocity-dependent, turbulent friction (friction coefficient ξ, units: m·s⁻²) (Bartelt et al., 1999). Retrospective analyses of glacier/ice avalanche events based on the VS model show that the best-fit frictional values generally range between 0.05 and 0.2 for μ, and between 1000 and 4000 m·s⁻² for ξ (Allen et al., 2009). Here in the modeling, we adopted moderate values of 0.15 and 2500 m·s⁻² for μ and ξ, respectively. We found that the maximum flow height is about 19 m and the runout distance is about 1.3 km (Fig. 12b), meaning the ice avalanche materials would not reach the Qinghai-Tibet railway with moderate friction coefficients.

To investigate how the altered frictional input parameters would influence the runout distance estimate, we also ran the VS model with multiple combinations of the parameter values (see Fig. 12c). It shows that the runout distance would be longer with decreasing μ and increasing ξ. Only when μ is lower than 0.06 and ξ is higher than 3000 m·s⁻², the collapse of the KLP-37 glacier tongue would pose a threat to the Qinghai-Tibet Railway (with a runout distance longer than 3 km). A small μ indicates low basal friction, and the best-fit value of μ for the Aru glaciers is 0.14 (Gilbert et al., 2018; Kääb et al., 2018). Compared with the flow velocity of Aru glaciers (~64.80±10.95 m·a⁻¹) before the collapse (Kääb et al., 2018), KLP-37 has a

Natural Hazards
and Earth System
Sciences
Discussions

Open Access

EGU

significantly slower flow velocity (see Section 4.3). We thus postulate that the realistic value of μ for the KLP-37 glacier is

460 unlikely higher than the threshold limit value (0.06) that will result in a hazardous runout distance (>3 km). Also, previous studies have shown that small μ values (<0.1) are mainly found at the collapse events occurring in the surging-type glaciers such as the Kolka glacier (Allen et al., 2009), which is not applicable to the KLP-37 glacier. Therefore, we suggest the avalanche of KLP-37 glacier tongue in the future, if it happens, will unlikely threaten the safety of the Qinghai-Tibet railway.

Note that we only considered the collapse of the KLP-37 glacier tongue in the modeling. The whole glacier may collapse under

465 extreme conditions such as heavy precipitation in a short time or the stimulation of strong earthquakes (Kääb et al., 2020), given the presence of extensive fissures in the upper glacier source region. For instance, the 2001 Mw7.8 earthquake on the Kunlun fault induced several ice avalanche events over the glaciers in the Kunlun Pass region (Jerome et al., 2004). Additionally, our modeling did not include the lubrication effects of fine-grained sediments under the glacier, which may reduce the avalanche friction and allow the detachments to accelerate particularly fast and cover long distances (Kääb et al.,

470 2020). It is thus essential to monitor the dynamics of the KLP-37 glacier continually in combination with elaborate numerical simulation to predict its potential hazardous impacts.

5.3 Implications for glacier collapse hazard monitoring and assessment

Although plenty of glaciers in QTP have been retreating in the last several decades, glacier advancing has been ubiquitously observed either on surge-type glaciers or on those experienced ice-rock collapses. Front line advancing is thus described as

475 important evidence of glacier instabilities (Kääb et al., 2020). In addition to this specific dynamic pattern, some communal geomorphic conditions have also been summarized from a compilation of 19 actual or possible glacier collapse events (Kääb et al., 2020). The most frequent geomorphic characteristics on these collapsed glaciers are found to be the presence of abundant weak bedrocks/fine sediments under a glacier and gentle surface slope ranging between about 10° and 20°. As discussed in Section 5.2, both the dynamic and geomorphic patterns of the KLP-37 glacier align with these previously identified common

480 conditions for a potential glacier collapse.

Our site-specific study of the KLP-37 glacier also adds the diversity of regional conditions for identifying collapse-prone glaciers. First, we found that the east branch of the KLP-37 glacier plays a key role in forming the ice-dammed lake, which in turn influences the dynamics of the glacier tongue of the west branch. This indicates that the unique glacier geometry modulated by local topography should be considered in identifying and assessing glacier collapse hazard. Second, the KLP-37 glacier is

485 located in a region where a few strong earthquakes have occurred in history. Note that the KLP-37 glacier tongue reaches a much lower elevation than the adjacent glaciers, which may lead to a hypothesis that the initial material deposition in the glacier tongue region (see the 1975 KH-9 image in Fig. 4a) was transported from the upper region by a historical seismic event. Given the triggering effect of large earthquakes on glacier collapse, particular attention should be paid to destabilized low-angle glaciers in active tectonic zones.

490 We have shown that using multi-source remote sensing images enables us to address the three-dimensional (i.e., horizontal

and vertical) dynamics of a glacier, which is particularly helpful for identifying collapse-prone glaciers. In the future, monitoring techniques with short temporal sampling rates such as ground-based SAR should be employed to capture the transient or accelerating signals of surface motion, which is vital for assessing the glacier stability. Our simulations of the potential runout distance of the KLP-37 glacier tongue provides an alternative solution for assessing the hazard influence of
495   an impending glacier collapse. We highlight that such modeling should be valued in the future because it is mostly the only way to give first-hand information on the possible glacier collapse influence.

6.   Conclusions

In this study, we analyzed the dynamics of a small low-angle valley glacier KLP-37 in the East Kunlun Mountains between 1975 and 2019 with multi-source remote sensing imagery, followed by a hazard assessment of the potential collapse of the
500   glacier tongue. We found that the glacier tongue has undergone slow surge-like processes in the recent four decades. The glacier snout has been progressively advancing during the observation period, with an accumulative advance distance of about 372±17.63 m. The glacier surface exhibited continuous thinning in the source region and thickening in the glacier tongue region. Negative volume changes were found over the glacier tongue region, indicating continuous loss of the glacier mass there. We observed an acceleration of the flow velocity of the glacier tongue, with the mean velocity below 4800 m almost
505   trebled, during the period 2009–2019.

Our observations suggest that several factors control the dynamics of the KLP-37 glacier. The change of flow direction of the glacier at an elevation of about 4800 m due to the local topography, coupled with the "V" shape of the glacier tongue geometry, presumably plays a crucial role for the surge-like behavior. The presence of an ice-dammed glacier lake and a supraglacial pond on the glacier tongue surface implies a hydrological influence on the glacier dynamics as well. Furthermore, the long-
510   term climate warming and increased annual precipitation likely enhance the glacier's dynamic intensities, as manifested by the abrupt increase of flow velocity after 2015.

The runout extent modeling using the Voellmy-Salm model suggests that the avalanche of the KLP-37 glacier tongue would unlikely influence the safety of the Qinghai-Tibet railway, given moderate friction parameters in the modeling. However, considering the presence of extensive fissures in the upper glacier source region, the whole glacier may collapse under extreme
515   conditions such as heavy precipitation in a short time or the stimulation of strong earthquakes. It is thus very essential to monitor the dynamics of the KLP-37 glacier continually in the future to ensure the operation safety of the Qinghai-Tibet railway and highway downstream.

This study also demonstrates the possibility of using multiple remotely sensed data to investigate the dynamics and morphological changes of glaciers in mountainous regions, where direct observations are scarce. Moreover, we have presented
520   a means of evaluating a destabilized glacier's runout hazard by employing numerical flow modeling based on remote sensing observations. The approach presented here for the KLP-37 glacier can be easily adapted for other similar mountain glaciers in vast regions to assist in collapse hazard prevention and mitigation.

Code availability

The open-source ASP software for generating the ASTER DEM based on the ASTER stereo images is available at
525 https://ti.arc.nasa.gov/tech/asr/groups/intelligent-robotics/ngt/stereo/. The HEXIMAP toolbox for extracting DEM from the declassified Hexagon KH-9 satellite imagery can be downloaded at https://github.com/gmorky/heximap. The MASSFLOW software for conducting the glacier collapse modeling is freely available at http://www.massflow-software.com/ for an educational purpose.

Data availability

530 The SRTM-C and Hexagon KH-9 images were downloaded from the United States Geological Survey (USGS) EROS Archive. The SRTM-X DEM and TanDEM were copyrighted by the German Aerospace Center. The HMA DEMs were downloaded from NASA National Snow and Ice Data Center Distributed Active Archive Center. The ASTER stereo images were downloaded from the NASA Earthdata Search archive. The Planet images were freely downloaded from the Planet website (https://www.planet.com/markets/education-and-research/) for scientific research purposes.

Author contribution

535 XW collected the satellite data, did most of the result analyses, and wrote the draft. LL and YH helped revise the manuscript. QL helped interpret the results. RZ and BZ helped pre-process some of the satellite data. TW, LZ, and GL supported the field trip to the study site in 2016. All the authors were involved in the editing of the manuscript.

Competing interests

540 The authors declare that they have no conflict of interest.

Acknowledgements

References

Allen, S.K., Schneider, D., and Owens, I.F.: First approaches towards modelling glacial hazards in the Mount Cook region of New Zealand's Southern Alps, Natural Hazards and Earth System Sciences, 9(2), 481–499, doi:10.5194/NHESS-9-481-2009, 2009.
550 Bai, X. and He, S.: Dynamic process of the massive Aru glacier collapse in Tibet, Landslides, 17(6), 1353–1361, doi:10.1007/s10346-019-01337-x, 2020.
Bartelt, P., Salm, B., and Gruber, U.: Calculating dense-snow avalanche runout using a Voellmy-fluid model with active/passive longitudinal straining, Journal of Glaciology, 45(150), 242–254, doi:10.1017/S002214300000174X, 1999.

555 Bhambri, R., Watson, C.S., Hewitt, K., Haritashya, U.K., Kargel, J.S., Pratap Shahi, A., Chand, P., Kumar, A., Verma, A., and Govil, H.: The hazardous 2017–2019 surge and river damming by Shispare Glacier, Karakoram, Sci Rep, 10(1), 4685, doi:10.1038/s41598-020-61277-8, , 2020.

Bolch, T., Pieczonka, T., and Benn, D.I.: Multi-decadal mass loss of glaciers in the Everest area (Nepal Himalaya) derived from stereo imagery, The Cryosphere, 5(2), 349–358, doi:10.5194/tc-5-349-2011, 2011.

560 Chen, D., Xu, B., Yao, T., Guo, Z., Cui, P., Chen, F., and Zhang, R.: Assessment of past, present and future environmental changes on the Tibetan Plateau, Chin Sci Bull, 60: 3025–3035, doi:10.1360/N972014-01370, 2015. (In Chinese)

Evans, S.G., Tutubalina, O.V., Drobyshev, V.N., Chernomorets, S.S., McDougall, S., Petrakov, D.A., and Hungr, O.: Catastrophic detachment and high-velocity long-runout flow of Kolka Glacier, Caucasus Mountains, Russia in 2002, Geomorphology, 105(3), 314–321, doi:10.1016/j.geomorph.2008.10.008, 2009.

565 Faillettaz, J., Funk, M., and Vincent, C.: Avalanching glacier instabilities: Review on processes and early warning perspectives, Reviews of Geophysics, 53(2), 203–224, doi:10.1002/2014rg000466, 2015.

Falaschi, D., Kääb, A., Paul, F., Tadono, T., Rivera, J.A., and Lenzano, L.E.: Brief communication: Collapse of 4Mm3 of ice from a cirque glacier in the Central Andes of Argentina, The Cryosphere, 13(3), 997–1004, doi:10.5194/tc-13-997-2019, 2019.

Farr, T.G., Rosen, P.A., Caro, E., Crippen, R., Duren, R., Hensley, S., Kobrick, M., Paller, M., Rodriguez, E., Roth, L., Seal, 570 D., Shaffer, S., Shimada, J., Umland, J., Werner, M., Oskin, M., Burbank, D., and Alsdorf, D.: The Shuttle Radar Topography Mission, Reviews of Geophysics, 45(2), 1–33, doi:10.1029/2005RG000183, 2007.

Gardelle, J., Berthier, E., Arnaud, Y., and Kääb, A.: Region-wide glacier mass balances over the Pamir-Karakoram-Himalaya during 1999–2011, The Cryosphere, 7(4), 1263–1286, doi:10.5194/tc-7-1263-2013, 2013.

Gilbert, A., Leinss, S., Kargel, J., Kääb, A., Gascoin, S., Leonard, G., Berthier, E., Karki, A., and Yao, T.: Mechanisms leading 575 to the 2016 giant twin glacier collapses, Aru Range, Tibet, The Cryosphere, 12(9), 2883–2900, doi:10.5194/tc-12-2883-2018, 2018.

Glen, J.W.: The creep of polycrystalline ice, Proceedings of the Royal Society: A Mathematical Physical and Engineering Sciences, 228(1175), 519–538, doi:10.1098/rspa.1955.0066, 1955.

Guo, W., Liu, S., Xu, L., Wu, L., Shangguan, D., Yao, X., Wei, J., Bao, W., Yu, P., Liu, Q., and Jiang, Z.: The second Chinese 580 glacier inventory: data, methods and results, Journal of Glaciology, 61, 357–372, doi: 10.3189/2015JoG14J209, 2015.

Haeberli, W., Huggel, C., Kääb, A., Zgraggen-Oswald, S., Polkvoj, A., Galushkin, I., Zotikov, I., and Osokin, N.: The Kolka-Karmadon rock/ice slide of 20 September 2002: An extraordinary event of historical dimensions in North Ossetia, Russian Caucasus, Journal of Glaciology, 50(171), 533–546, doi:10.3189/172756504781829710, 2004.

Hall, D.K., Bayr, K.J., Schöner, W., Bindschadler, R.A., and Chien, J.Y.L.: Consideration of the errors inherent in mapping 585 historical glacier positions in Austria from the ground and space (1893-2001), Remote Sensing of Environment, 86(4), 566–577, doi:10.1016/S0034-4257(03)00134-2, 2003.

Hirano, A., Welch, R., Lang, H.: Mapping from ASTER stereo image data: DEM validation and accuracy assessment, ISPRS Journal of Photogrammetry and Remote Sensing, 57(5), 356–370, doi:10.1016/S0924-2716(02)00164-8, 2003.

Huggel, C., Zgraggen-Oswald, S., Haeberli, W., and Kääb, A.: The 2002 rock/ice avalanche at Kolka/Karmadon, Russian 590 Caucasus: assessment of extraordinary avalanche formation and mobility, and application of QuickBird satellite imagery, Nature Hazard and Earth System Science, 5, 173–187, doi:10.5194/nhess-5-173-2005, 2005.

Huss, M. and Farinotti, D.: Distributed ice thickness and volume of all glaciers around the globe, Journal of Geophysical research, 117, F04010, doi:117 10.1029/2012JF002523, 2012.

Jaber, W., Floricioiu, D., Rott, H., Eineder, M.: Surface elevation changes of glaciers derived from SRTM and TanDEM-X 595 DEM differences, IEEE International Geoscience and Remote Sensing Symposium, (IGARSS) 2013, Melbourne, VIC, pp. 1893–1896, doi:10.1109/IGARSS.2013.6723173, 2013.

Jacquemart, M., Loso, M., Leopold, M., Welty, E., Berthier, E., Hansen, J.S.S., Sykes, J., and Tiampo, K.: What drives large-

Natural Hazards
and Earth System
Sciences
Discussions

scale glacier detachments? Insights from Flat Creek glacier, St. Elias Mountains, Alaska, Geology, 48(7), 703–707, doi:10.1130/g47211.1, 2020.

600 Jerome, V. D. W., Owen, L. A., Tapponnier, P., Xu, X., Kervyn, F., Finkel, R. C., and Barnard, P. L.: Giant, ~ M8 earthquake-triggered ice avalanches in the eastern Kunlun Shan, northern Tibet: Characteristics, nature and dynamics, Geological Society of America Bulletin, 116(3): 394–406. https://doi.org/10.1130/B25317.1, 2004.

Kääb, A., Jacquemart, M., Gilbert, A., Leinss, S., Girod, L., Huggel, C., Falaschi, D., Ugalde, F., Petrakov, D., Chernomorets, S., Dokukin, M., Paul, F., Gascoin, S., Berthier, E., Kargel, J.: Sudden large-volume detachments of low-angle mountain
605 glaciers–more frequent than thought, The Cryosphere Discussions, doi:10.5194/tc-2020-243, 2020.

Kääb, A., Leinss, S., Gilbert, A., Bühler, Y., Gascoin, S., Evans, S.G., Bartelt, P., Berthier, E., Brun, F., Chao, W.-A., Farinotti, D., Gimbert, F., Guo, W., Huggel, C., Kargel, J.S., Leonard, G.J., Tian, L., Treichler, D., and Yao, T.: Massive collapse of two glaciers in western Tibet in 2016 after surge-like instability, Nature Geoscience, 11(2), 114–120, doi:10.1038/s41561-017-0039-7, 2018.

610 Kotlyakov, V.M., Rototaeva, O.V., Nosenko, G.A.: The September 2002 Kolka Glacier catastrophe in North Ossetia, Russian Federation: evidence and analysis, Mountain Research and Development, 24(1): 78–83, doi:10.1659/0276-4741(2004)024[0078:Tskgci]2.0.Co;2, 2004.

Krieger, G., Moreira, A., Fiedler, H., Hajnsek, I., Werner, M., Younis, M., and Zink, M.: TanDEM-X: A Satellite formation for high-resolution SAR interferometry. IEEE Transactions on Geoscience and Remote Sensing, 45(11), 3317–3341,
615 doi:10.1109/TGRS.2007.900693, 2007.

Lambrecht, A., Mayer, C., Aizen, V., Floricioiu, D., and Surazakov, A.: The evolution of Fedchenko glacier in the Pamir, Tajikistan, during the past eight decades, Journal of Glaciology, 60(220), 233–244, doi:10.3189/2014JOG13J110, 2014.

Lasserre, C., Peltzer, G., Crampé, F., Klinger, Y., Van der Woerd, J., and Tapponnier, P.: Coseismic deformation of the 2001 Mw = 7.8 Kokoxili earthquake in Tibet, measured by synthetic aperture radar interferometry, J. Geophys. Res., 110,
620 B12408, doi:10.1029/2004JB003500, 2005.

Leinss, S., Willimann, C., and Hajnsek, I.: Glacier detachment hazard analysis in the West Kunlun Shan mountains. IEEE International Geoscience and Remote Sensing Symposium (IGARSS) 2019, Yokohama, Japan, pp. 4565–4568, doi:10.1109/IGARSS.2019.8900320, 2019.

Li, J., Li, Z.W., Zhu, J.J., Li, X., Xu, B., Wang, Q.J., Huang, C.L., and Hu, J.: Early 21st century glacier thickness changes in
625 the Central Tien Shan, Remote Sensing of Environment, 192, 12–29, doi:10.1016/j.rse.2017.02.003, 2017.

Luo, J., Niu, F.J., Lin, Z.J., Liu, M.H., and Yin, G.A.: Variations in the northern permafrost boundary over the last four decades in the Xidatan region, Qinghai–Tibet Plateau, Journal of Mountain Science, 15(4), 765–778, doi:10.1007/s11629-017-4731-2, 2018.

Maurer, J.M., Rupper, S.B., and Schaefer, J.M.: Quantifying ice loss in the eastern Himalayas since 1974 using declassified
630 spy satellite imagery, The Cryosphere, 10(5), 2203–2215, doi:10.5194/TC-10-2203-2016, 2016.

McNabb, R., Nuth, C., Kääb, A., and Girod, L.: Sensitivity of glacier volume change estimation to DEM void interpolation, The Cryosphere, 13(3), 895–910, doi:10.5194/tc-13-895-2019, 2019.

Murray, T., Strozzi, T., Luckman, A., Jiskoot, H., and Christakos, P.: Is there a single surge mechanism? Contrasts in dynamics between glacier surges in Svalbard and other regions, J. Geophys. Res., 108, 2237, doi:108 10.1029/2002JB001906, 2003.

635 Nuth, C. and Kääb, A.: Co-registration and bias corrections of satellite elevation data sets for quantifying glacier thickness change, The Cryosphere, 5(1), 271–290, doi:10.5194/tc-5-271-2011, 2011.

Ouyang, C., He, S., Xu, Q., Luo, Y., and Zhang, W.: A MacCormack-TVD finite difference method to simulate the mass flow in mountainous terrain with variable computational domain, Computers & Geosciences, 52, 1–10, doi:10.1016/j.cageo.2012.08.024, 2013.

640 Paul, F.: Repeat glacier collapses and surges in the Amney Machen Mountain Range, Tibet, possibly triggered by a developing rock-slope instability, Remote Sensing, 11(6), 708, doi:10.3390/rs11060708, 2019.

Natural Hazards
and Earth System
Sciences
Discussions

Rashid, I., Majeed, U., Jan, A., and Glasser, N.F.: The January 2018 to September 2019 surge of Shisper Glacier, Pakistan, detected from remote sensing observations, Geomorphology, 351, 105394, doi:10.1016/j.geomorph.2019.106957, 2020.

645   Riegler, G., Hennig, S.D., and Weber, M.: WORLDDEM–a novel global foundation layer, ISPRS International Archives of the Photogrammetry Remote Sensing and Spatial Information Sciences, Munich, Germany, pp. 183–187, doi:10.5194/isprsarchives-xl-3-w2-183-2015, 2015.

Rosu, A.M., Pierrot-Deseilligny, M., Delorme, A., Binet, R., and Klinger, Y.: Measurement of ground displacement from optical satellite image correlation using the free open-source software MicMac, ISPRS Journal of Photogrammetry and Remote Sensing, 100, 48–59, doi:10.1016/j.isprsjprs.2014.03.002, 2015.

650   Rupnik, E., Daakir, M., and Pierrot Deseilligny, M.: MicMac – a free, open-source solution for photogrammetry, Open Geospatial Data, Software and Standards, 2(1), 14. 10.1186/s40965-017-0027-2, 2017.

Sakai, A.: Brief communication: Updated GAMDAM glacier inventory over high-mountain Asia, The Cryosphere, 13(7), 2043–2049, doi:10.5194/tc-13-2043-2019, 2019.

Scherler, D., Bookhagen, B., and Strecker, M.R.: Spatially variable response of Himalayan glaciers to climate change affected
655   by debris cover, Nature Geoscience, 4(3), 156–159, doi:10.1038/ngeo1068, 2011.

Shean D.: High Mountain Asia 8-meter DEMs derived from along-track optical imagery, NASA National Snow and Ice Data Center Distributed Active Archive Center, doi:10.5067/gsacb044m4pk, 2017.

Shean, D.E., Alexandrov, O., Moratto, Z.M., Smith, B.E., Joughin, I.R., Porter, C., and Morin, P.: An automated, open-source pipeline for mass production of digital elevation models (DEMs) from very-high-resolution commercial stereo satellite
660   imager, ISPRS Journal of Photogrammetry and Remote Sensing, 116, 101–117, doi:10.1016/j.isprsjprs.2016.03.012, 2016.

Tian, L., Yao, T., Gao, Y., Thompson, L., Mosley-Thompson, E., Muhammad, S., Zong, J., Wang, C., Jin, S., and Li, Z.: Two glaciers collapse in western Tibet, Journal of Glaciology, 63(237), 194–197, doi:10.1017/jog.2016.122, 2016.

Wang X., Liu Q., Zhang B., Zhang R., and Liu G.: Monitoring and analyzing collapse of KLSK-37 glacier tongue in recent 40 years with multi-source remote sensing, Geomatics and Information Science of Wuhan University, 45(11): 1687–1696.
665   doi: 10.13203/j.whugis20200214, 2020. (In Chinese)

Wessel, P., Smith, W.H.F., Scharroo, R., Luis, J., and Wobbe, F.: Generic Mapping Tools: improved version released, Eos Trans. AGU, 94(45): 409–410, doi:10.1002/2013EO450001, 2013.

Wendt, A., Mayer, C., Lambrecht, A., and Floricioiu, D.: A Glacier Surge of Bivachny Glacier, Pamir Mountains, Observed by a Time Series of High-Resolution Digital Elevation Models and Glacier Velocities, Remote Sensing, 9(4), 388,
670   doi:10.3390/rs9040388, 2017.

Wu, T., Li, S., Cheng, G., and Nan, Z.: Using ground-penetrating radar to detect permafrost degradation in the northern limit of permafrost on the Tibetan Plateau, Cold Regions Science and Technology, 41(3), 211–219 (In Chinese), doi:10.1016/j.coldregions.2004.10.006, 2005.

Wu, X.H., Qian, F., and Pu Q.Y.: Quaternary Geology of the Eastern Kunlun Mountain, Symposium of Geology on Tibetan
675   Plateau, pp. 1-18. Beijing: Geological Publishing House, 1982. (In Chinese)

Yasuda, T. and Furuya, M.: Dynamics of surge-type glaciers in West Kunlun Shan, Northwestern Tibet. Journal of Geophysical Research: Earth Surface, 120(11), 2393–2405, doi:10.1002/2015jf003511, 2015.

Yue, G., Zhao, L., Zhao, Y., Du, E., Wang, Q., Wang, Z., and Qiao, Y.: Relationship between soil properties in permafrost active layer and surface vegetation in Xidatan on the Qinghai-Tibetan plateau, Journal of Glaciology and Geocryology,
680   35(3), 565–573, 2013. (In Chinese)

Table 1. Satellite imagery and DEMs used in this study.

Data	Date	Spatial Resolution (m)	Data type	Purpose
RapidEye	2009/08/30; 2010/09/07; 2012/09/12; 2013/08/04; 2015/10/12;	5	Orthoimages	Geomorphic change Terminus advance
PlanetScope	2016/09/10; 2017/08/09; 2018/07/24; 2019/08/06	3	Orthoimages	Flow velocity
Google Earth	2013/08/15	~ 1	-	Geomorphic change
KH-9	1975/12/10	7.6	Stereo images	Terminus advance Elevation change
ASTER	2018/01/12	15	Stereo images	Elevation change
SRTM-X/C	2002/02	30	DEM	Elevation change
HMA DEM	2010/12/05; 2014/08/27	8	DEM	Elevation change
TanDEM-X	2011–2014	12	DEM	GCP elevation Elevation reference

Table 2. Net volume changes over the glacier tongue region calculated from the four DEM pairs.

DEM pairs	Time span (years)	Net volume change ($\times 10^5$ m³)
KH-9–SRTM	24.2	-1.54±1.18
SRTM–HMA10	10.8	-5.74±1.47
HMA10–HMA14	3.73	-0.49±0.11
HMA14–ASTER	3.38	-3.44±1.87